ADVANCED OPTICAL MATERIALS
www.advopticalmat.de

Temperature-Dependent Excitonic Band Gap in Lead-Free Bismuth Halide Low-Dimensional Perovskite Single Crystals

Salvatore Valastro, Stevan Gavranovic, Ioannis Deretzis, Martin Vala, Emanuele Smecca, Antonino La Magna, Alessandra Alberti, Klara Castkova, and Giovanni Mannino*

In this study, the optical behavior of lead-free Bi-based low-dimensional perovskite single crystals ($Cs_3Bi_2Cl_9$, $Cs_3Bi_2Br_9$, $Cs_3Bi_2I_9$, and $MA_3Bi_2I_9$) is investigated by spectroscopic ellipsometry, supported by X-ray diffraction and density functional theory calculations. All materials exhibit a strong excitonic peak resulting from photogenerated electron–hole Coulomb interactions, whereas the threshold of continuous absorption is found at higher energies. The resonances of the excitonic and continuous bands, along with exciton binding energies, are extracted through Critical Point Analysis of the ellipsometric data over a wide temperature range (from −90 °C to 90 °C), revealing subtle variations in the optical characteristics for each single crystal. These materials can be applied in optoelectronics as photodetectors because of their high stability and lower toxicity compared to their Pb-based perovskites.

1. Introduction

In recent years, halide perovskites have demonstrated outstanding potential in the field of optoelectronics where they have been employed as active materials in diverse applications including solar cells,[1] light-emitting diodes (LEDs),[2] photodetectors,[3] memristors[4,5] and more. The extensively studied perovskite materials predominantly feature the lead cation (Pb^{2+}).[6] One approach to prevent its leakage and environmental contamination involves designing an adsorbing layer capable of accumulating leaked material in the event of breaks and mechanical failures.[7] The alternative is to substitute Pb^{2+} in the crystalline lattice of halide perovskites. This approach aims to replace Pb^{2+} with an environmentally acceptable counterpart while retaining the properties of lead halide perovskites (large optical absorption coefficient,[8–11] tunable band gap,[12,13] low trap densities,[14–16] high charge carrier mobilities,[17,18] long diffusion lengths[19] and lifetimes[20]) and enhancing their moisture stability.[21] There are essentially two alternatives for lead replacement:[22] homovalent substitutions where every Pb^{2+} is replaced with a divalent cation, and heterovalent substitution where every two Pb^{2+} cations are replaced by either ion-splitting (e.g., substitution by one monovalent and one trivalent cation, or mixed chalcogen and halogen elements) or vacancy-ordered formation using post-transition metals. Homovalent metal cation substitution (e.g., with Ge^{2+} or Sn^{2+}) typically leads to the formation of lattice distortion for ABX_3 perovskites (A = Cs^+, MA^+, FA^+, B = Pb^{2+}, Sn^{2+}, Ge^{2+} and X = Cl^-, Br^- or I^-). The formation of vacancies and the distortion of the $ASnX_3$ perovskite structure mainly occur due to the oxidation tendency of Sn ($Sn^{2+} \rightarrow Sn^{4+}$) caused by the unstable high-energy-lying $5s^2$ states.[23,24] Therefore, Sn-based perovskites exhibit low stability in air and moisture.[25] On the contrary, the origin of lattice distortion of Ge-based perovskites lies in a significant ionic radius difference between Ge^{2+} (0.73 Å) and Pb^{2+} (1.19 Å), due to which Ge^{2+} cannot form stable GeI_6^{4-} octahedra.[26] Heterovalent substitution by ion-splitting and vacancy-ordered formation offers a wide diversity of stable perovskite and perovskite-like structures (e.g., $A_2B^+B^{3+}X_6$,[27–29] $A_3\square B^{3+}{}_2X_9$,[30] where □ represents the vacancy).

The non-toxic bismuth cation (Bi^{3+}) emerged as one of the most suitable lead counterparts for heterovalent substitution. This is primarily because Bi^{3+} shares the same $6s^26p^0$ electronic structure as the Pb^{2+} cation and has a similar effective ionic radius (1.03 Å).[31] Additionally, Bi-based perovskites have shown superior moisture and thermal stability.[32] One of the promising Bi-based perovskite structures is the $A_3Bi_2X_9$, formed by hexagonal or cubic packing of A and X cations. Whereas the trivalent Bi^{3+} cations occupy only two-thirds of the octahedral cavities BiX_6.[33] Unlike the 3D framework made up of corner-sharing PbX_6 octahedra present in $APbX_3$, the crystalline lattice

S. Valastro, I. Deretzis, E. Smecca, A. La Magna, A. Alberti, G. Mannino
Institute for Microelectronics and Microsystems (IMM)
National Research Council (CNR)
Strada VIII n.5 Zona Industriale, Catania 95121, Italy
S. Gavranovic, M. Vala
Faculty of Chemistry
Materials Research Centre
Brno University of Technology
Purkynova 118, Brno 612 00, Czech Republic
E-mail: xcgavranovic@vutbr.cz
K. Castkova
Central European Institute of Technology (CEITEC)
Brno University of Technology
Purkynova 656/123, Brno 612 00, Czech Republic
The ORCID identification number(s) for the author(s) of this article can be found under https://doi.org/10.1002/adom.202302397

DOI: 10.1002/adom.202302397

of $A_3Bi_2X_9$ Bi-based alternatives is determined by various stackings of trigonal AB_3 layers.

In principle, there are three types of stackings present in these structures: h, hcc, and c.[34] The hexagonal $(h)_6$ stacking leads to the formation of rhombohedral structures with a 0D framework of face-sharing Bi-X octahedra, i.e., the framework of isolated bi-octahedral $B_2X_9^{3-}$ anions. When stacked in cubic (c) mode, they form trigonal structures, where BiX_6 octahedra share cis-vertices with the other three octahedra and thus create the 2D corrugated layers. The $(hcc)_2$ stacking leads to the formation of hexagonal and orthorhombic structures, where both kinds of octahedron bonding, i.e., both 0D and 2D structures are possible.[33,34]

Previous reports show that $Cs_3Bi_2I_9$ and $MA_3Bi_2I_9$ crystallize in hexagonal structure ($P6_3/mmc$)[35–37] with the 0D motive of bi-octahedra, while $Cs_3Bi_2Br_9$ crystallizes in trigonal ($P\bar{3}m1$)[38,39] and $Cs_3Bi_2Cl_9$ in either orthorhombic (Pnma)[40,41] or trigonal ($P\bar{3}1c$)[42] crystal systems (space groups), with the 2D motive of $BiBr_6$ and $BiCl_6$ octahedra, respectively. Due to the reduced dimensionality, $A_3Bi_2X_9$ perovskites have relatively large band gap (1.94–3.02 eV)[36,41,42] and extremely low ionic migration. The thin films of $Cs_3Bi_2I_9$ and $MA_3Bi_2I_9$ have been used as photoactive layers in solar cells while $Cs_3Bi_2Br_9$ and $Cs_3Bi_2Cl_9$ were not used in solar devices due to the too-wide electronic band gap.[43] However, these Bi-based perovskites exhibit low dark current noise (at pA level) and high resistivity (up to 10^{12} Ω cm)[36] both very desirable properties for the construction of highly sensitive photodetectors. Additionally, these non-toxic materials showed outstanding thermal stability, fast response speeds (in milliseconds) and high signal-to-noise (on–off) ratio. Li et. al.,[44] presented the vertical ITO/$Cs_3Bi_2I_9$/Au photodetectors with an exceptional on-off ratio of 11 000, measured under −2 V bias and a white LED of 100 mW cm^{-2} light intensity. Moreover, these devices showed great long-term stability, preserving more than 90% of their initial response after 1000 h of exposure to humid air (50% RH). $MA_3Bi_2I_9$ also proved to be a suitable material for efficient photodetection. Hussain et. al.[45] fabricated Ag/$MA_3Bi_2I_9$/FTO photodetector with high detectivity (1.3×10^{12} Jones) and a fast response speed of (26.81/41.98 ms) under 0 V bias and low white light intensity of 10 μW cm^{-2}. Furthermore, $Cs_3Bi_2I_9$ demonstrated great potential for X-ray detection.[46] Zhang et. al.[47] reported X-ray detectors based on centimeter-sized $Cs_3Bi_2I_9$ single crystals, which exhibited a high sensitivity of 1652.3 μC $Gy_{air}^{-1}cm^{-2}$ and a very low detection limit of 130 nGy_{air} s^{-1} ≈4 times higher than α-Se detectors and ≈40 times lower than required for medical diagnostics. Additionally, these single crystals showed outstanding operational stability, even at a higher temperature of 100 °C.

Unlike their iodide counterparts, $Cs_3Bi_2I_9$ and $MA_3Bi_2I_9$, the research on the detection potential of $Cs_3Bi_2Br_9$ and $Cs_3Bi_2Cl_9$ is still in its infancy. Liu et. al.[48] demonstrated the detecting capability of a self-powered FTO/NiO_x/$Cs_3Bi_2Br_9$/Au UV photodetector, with a fast response speed of 3.04/4.65 ms, the responsivity of 4.33 mA W^{-1} and detectivity of 1.3×10^{11} Jones (measured under week UV light of 15 mW cm^{-2}, 405 nm). Tailor et al.[41] reported the first Ag/$Cs_3Bi_2Cl_9$/Ag detectors with a responsivity of 17 mA W^{-1} and detectivity as high as 6.63×10^{11} Jones. Although these materials show significant response to incident photons, the relationship between their optical properties and device performance is not fully explained.

Before contemplating their potential application in optoelectronics (photodetectors, scintillators, solar cells etc.), it is crucial to comprehend how the optical properties of these materials evolve concerning temperature, chemical composition, dimensionality, and how such changes could impact the performance of future $A_3Bi_2X_9$-based devices. In this work, we report an extensive multi-material study of the band gap change for inorganic and hybrid $A_3Bi_2X_9$ perovskite single crystals ($Cs_3Bi_2Cl_9$, $Cs_3Bi_2Br_9$, $Cs_3Bi_2I_9$, and $MA_3Bi_2I_9$) using spectroscopic ellipsometry (SE), supported by x-ray diffraction and density functional theory (DFT) calculations. We identified the interband transition energies by applying a Critical Point (CP) Analysis on the absorption spectra, to gain a comprehensive understanding of the excitonic processes in the 1–5 eV energy range, considering temperature variations that span from −90 °C to 90 °C. Within this framework, we discuss exciton and continuous band absorption, phase changes and fine differences in the optical properties arising from the chemical and structural differences of the studied materials.

2. Results and Discussion

Figure 1a,d shows the optical photograph of the as-prepared single crystals. Figure 1e,h displays the X-Ray Diffraction (XRD) patterns acquired in $\vartheta-2\vartheta$ configuration at room temperature (RT) along with the relative 2D lattice scheme in the inset for all four Bi-based perovskite single crystals. The $Cs_3Bi_2Cl_9$ XRD pattern shows three peaks at 9.4°, 18.9° and 28.7° ascribed to (200), (400), (600) planes of a "quasi 1D-structure" orthorhombic phase[41] (Figure 1e; Table S2, Supporting Information). The $Cs_3Bi_2Br_9$ XRD pattern is characterised by five peaks at 12.8°, 15.6°, 25.8°, 27.3°, and 31.6° ascribed to (100), (101), (200), (201) and (202) planes, respectively, identifying a "quasi 2D-structure" trigonal phase (Figure 1f; Table S2, Supporting Information). The XRD patterns of the two crystals having iodine as anion ($Cs_3Bi_2I_9$ and $MA_3Bi_2I_9$) share similar features with 2 peaks at 16.6° and 25.2° indicating the (004) and (006) planes of a "quasi 0D-structure" hexagonal phase (Figure 1g,h; Table S2, Supporting Information). Experimental lattice parameters of $Cs_3Bi_2Cl_9$ (a), $Cs_3Bi_2Br_9$ (b), $Cs_3Bi_2I_9$ (c), and $MA_3Bi_2I_9$ single crystal compared to theoretical values are reported in Table S3 and Figure S6 (Supporting Information).

We point out that, although the $Cs_3Bi_2Br_9$ sample presents more than one set of planes, only the most intense set was selected for SE measurements. On the other hand, we attempted to use a more refined optical model that take into account the anisotropy without obtaining a fitting improvement, very likely due to the very low contribution (i.e., intensity) of other planes to the optical response.

To investigate the optical properties of Bi-based crystals, we performed SE measurements at room temperature (RT) and in air on all the as-prepared samples. The experimental data fit and the extracted dielectric function, as discussed in the experimental section, are shown in Figure S7 (Supporting Information).

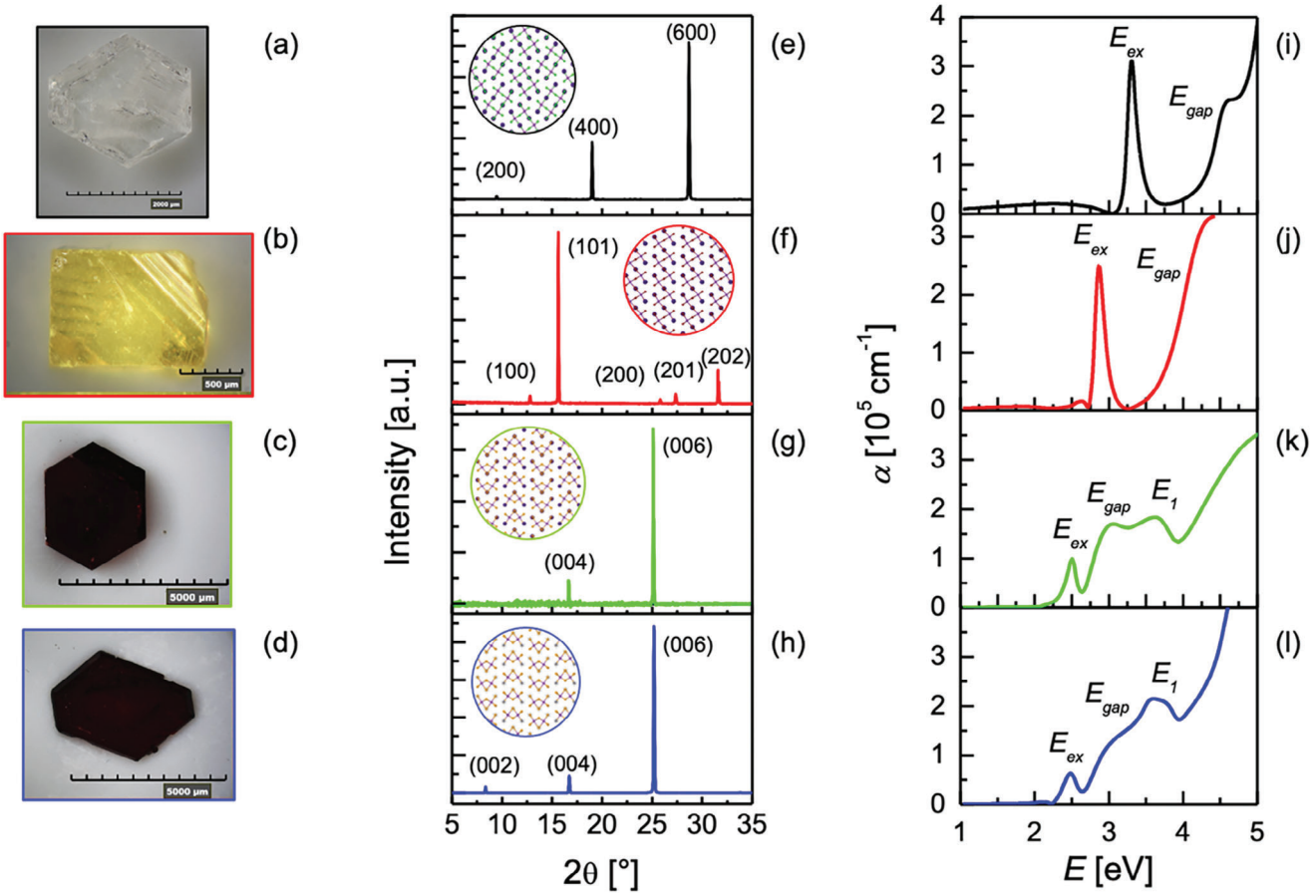

Figure 1. a–d) Optical photograph of $Cs_3Bi_2Cl_9$ (a), $Cs_3Bi_2Br_9$ (b), $Cs_3Bi_2I_9$ (c), $MA_3Bi_2I_9$ (d) single crystals. e–h) XRD patterns acquired in symmetrical ϑ-2ϑ configuration at RT and the relative 2D-scheme of the lattice as an inset for $Cs_3Bi_2Cl_9$ (e), $Cs_3Bi_2Br_9$ (f), $Cs_3Bi_2I_9$ (g), $MA_3Bi_2I_9$ (h). Color for atoms/molecules: pink=Bi, purple=Cs, green=Cl, red=Br, white=MA, yellow=I. i–l) Absorption coefficient of $Cs_3Bi_2Cl_9$ (i), $Cs_3Bi_2Br_9$ (j), $Cs_3Bi_2I_9$ (k), $MA_3Bi_2I_9$ (l) measured by spectroscopic ellipsometry.

Figure 1i,l shows the absorption coefficient calculated from the real (ϵ_1) and the imaginary (ϵ_2) parts of the dielectric function using equation:[49]

$$\alpha = \frac{2E}{c\hbar}\sqrt{\frac{\sqrt{\epsilon_1^2+\epsilon_2^2}-\epsilon_1}{2}} \quad (1)$$

where E is the energy, c is the speed of light in vacuum and h is the Planck constant. The absorption coefficient increases abruptly at a certain energy value that, when excitons are absent, or too weakly bounded, corresponds to the onset of the continuous band and characterizes the band gap (E_{gap}) of the system. In materials where bound excitons are present, the difference between the exciton energy (E_{ex}) and the E_{gap} defines the exciton binding energy $E_B = E_{gap} - E_{ex}$.[50] In all Pb-based perovskite materials like $MAPbI_3$,[51] $MAPbBr_3$,[11] $CsPbI_3$,[52] $CsPbBr_3$,[11] E_{ex} is hardly distinguishable from E_{gap} due to low exciton binding energies (25–50 meV[53]). In these materials (bulk or thin layers), the exciton is easily separated in free charges, making them good candidates for solar cell devices.[50] On the contrary, in all studied Bi-based materials, we observe an isolated and narrow excitonic peak, indicated as E_{ex} in Figure 1i,l. This peak is more prominent for the $Cs_3Bi_2Br_9$ and $Cs_3Bi_2Cl_9$ systems with respect to the two iodides ($Cs_3Bi_2I_9$ and $MA_3Bi_2I_9$). We argue that this peak arises from electron–hole interactions and reflects a bound exciton owing to a large binding energy at RT,[54–56] while E_{gap} is located at higher energy (Figure 1i,l). For this reason, if the material's band gap is set to the excitonic absorption onset, its value is by far underestimated. This feature was previously reported in the literature for $Cs_3Bi_2I_9$[57] and $MA_3Bi_2I_9$[58] single crystals, but only for $Cs_3Bi_2Cl_9$[41,42,59] and $Cs_3Bi_2Br_9$[60–63] nanosystems. For the two latter materials, it is possible to find optical characterizations in the literature that refer to nanocrystals or nanoplatelets, where quantum confinement effects and surface-related phenomena might affect the data with respect to the large single crystals used here.[64]

The absorption coefficient provides also information about defects. In particular, the $Cs_3Bi_2Cl_9$ (Figure 1a) and $Cs_3Bi_2Br_9$ (Figure 1b) and to a very lesser extent also $MA_3Bi_2I_9$ (d) have defects inside the gap attested by the broad band at energies just below the excitonic peak. We also calculated the Urbach tail at the band edge according to the following equation $\alpha = \alpha_0 \exp(E/E_u)$ where α_0 is a constant, E is the energy and E_u is the Urbach energy. The values of E_u are 33 meV for $Cs_3Bi_2Cl_9$, 20 meV for $Cs_3Bi_2Br_9$, 96 meV for $Cs_3Bi_2I_9$, and 34 meV for $MA_3Bi_2I_9$.

Table 1. Energy values of E_{ex}, E_{gap} and E_1 at RT extracted through the Critical Points analysis for $Cs_3Bi_2Cl_9$, $Cs_3Bi_2Br_9$, $Cs_3Bi_2I_9$, and $MA_3Bi_2I_9$. E_B (the exciton binding energy) is calculated as $E_{gap} - E_{ex}$.

Chemical formula	E_{ex} [eV]	E_{gap} [eV]	E_1 [eV]	E_B [meV]
$Cs_3Bi_2Cl_9$	3.277 ± 0.001	4.42 ± 0.03	\	1143
$Cs_3Bi_2Br_9$	2.836 ± 0.001	4.26 ± 0.03	\	1424
$Cs_3Bi_2I_9$	2.538 ± 0.001	2.87 ± 0.01	3.83 ± 0.03	334
$MA_3Bi_2I_9$	2.510 ± 0.004	2.81 ± 0.02	3.68 ± 0.02	303

In **Table 1**, we report the energy values of E_{ex}, E_{gap} and the first interband transition (E_1) common to all the Bi-based crystals at RT extracted through the Critical Point (CP) Analysis of the SE data as reported by Cardona and co-workers.[65–72] The CPs, which depend on the densities of states in the electronic bands, and their parameters (energy position E, amplitude A, broadening Γ, and phase Φ) are extracted from the simultaneous fit of the real and imaginary parts of the dielectric function (ϵ) through the following equation:

$$\frac{\partial^2 \epsilon}{\partial \omega^2} = n(n-1) A e^{i\Phi} (\omega - E + i\Gamma)^{(n-2)} \quad (2)$$

where n is −1/2 for 1D, 0 for 2D, or ½ for 3D critical points and −1 when describing excitonic transitions. The E_{ex} and E_{gap} values calculated for $Cs_3Bi_2Cl_9$ and $Cs_3Bi_2Br_9$, have not been yet reported in the literature and are respectively: 3.27 and 4.42 eV for $Cs_3Bi_2Cl_9$, and 2.84 and 4.26 eV for $Cs_3Bi_2Br_9$. On the other hand, E_{ex} and E_{gap} values for $Cs_3Bi_2I_9$ and $MA_3Bi_2I_9$ confirm the values reported by Machulin et al.[57] ($Cs_3Bi_2I_9$, calculated by reflection spectra at RT, 2.578 and 2.857 eV) and by Kawai et al.[58] ($MA_3Bi_2I_9$, calculated by absorption spectra at RT, 2.49 and 2.9 eV).

$Cs_3Bi_2Cl_9$ and $Cs_3Bi_2Br_9$ exhibit a large E_B of 1143 meV and 1424 meV, respectively. The value obtained for $Cs_3Bi_2Br_9$ is higher than those reported by Bass et al.[54] from UV–vis absorption measurements performed on powder (940 meV) and by Wu et al. from similar measurements on nanoplatelets (148 meV),[73] indicating a strong dependence of the optical properties of the material from the characteristics of the crystal structure.

The exciton binding energies for $Cs_3Bi_2I_9$ (334 meV) and $MA_3Bi_2I_9$ (303 meV) are close to those already reported.[57,58] These high values of E_B (not efficient charge separation resulting in low J_{SC}[74]), along with the wide electronic band gap (low optical absorption) and high Urbach energy (≈50 meV, resulting in high nonradiative recombination losses[75]), are the main reasons for the low values of photo-conversion efficiency reached using $Cs_3Bi_2I_9$ and $MA_3Bi_2I_9$ as active materials in solar cells (record of 3.6%[76] and 3.17%,[77] respectively).

Table 2. Energy values of E_{gap}, E_B at RT extracted through the Elliot Analysis for $Cs_3Bi_2Cl_9$, $Cs_3Bi_2Br_9$, $Cs_3Bi_2I_9$, and $MA_3Bi_2I_9$. The E_{ex} (the exciton energy) is calculated as $E_{gap} - E_B$.

Chemical formula	E_{ex} [eV]	E_{gap} [eV]	E_B [meV]
$Cs_3Bi_2Cl_9$	3.32 ± 0.02	4.40 ± 0.02	1080
$Cs_3Bi_2Br_9$	2.88 ± 0.01	4.26 ± 0.01	1380
$Cs_3Bi_2I_9$	2.44 ± 0.01	2.77 ± 0.01	340
$MA_3Bi_2I_9$	2.49 ± 0.01	2.79 ± 0.01	310

These results can be compared to those calculated with the Elliot model[78–81] used to simulate the absorption near the band edge with the equation:

$$Abs(E) = A_c \cdot \left(1 + \mathrm{erf}\left(\gamma \cdot \left(E - E_{gap}\right)\right)\right) + \sum_{n=1}^{3} \frac{\beta}{n^3} \cdot \exp\left(\frac{-\left(E - E_{gap} + \frac{E_B}{n^2}\right)^2}{\sigma^2}\right) \quad (3)$$

where E_{gap} is the electronic band gap, E_B is the exciton binding energy (i. e. $E_B = E_{gap} - E_{ex}$ where E_{ex} is the energy of the exciton), A_c, β, γ, σ are the scaling factors. The first term describes the continuum state absorption and the second term accounts for multiple excitonic states. We neglect the excitonic transition with n>3 because the excitonic peak is well separated from continuous and the oscillator strength decreases as n^3. The cumulative fit is in good agreement with experimental data as shown in Figure S8 (Supporting Information). The values obtained from fitting are reported in **Table 2**.

To further investigate the optical behavior of Bi-based crystals as a function of the temperature, being aware that other perovskitic materials are very sensitive to external factors like humidity that affect their properties, we have performed SE measurements in a pure N_2 environment, to avoid possible sample degradation.[82,83] Repeated measurements have demonstrated that all samples are stable in N_2 for several weeks. The measurements were performed in the range of −90 °C to 90 °C, to cover all the possible application fields, from x-ray and gamma detectors, which can work at low temperatures to minimize the dark current to LED and solar cells that can reach high working temperatures under sunlight.[84]

The variation of the absorption coefficient as a function of temperature is reported in Figure S9 (Supporting Information).

The E_{ex} and E_{gap} temperature dependence of $Cs_3Bi_2I_9$ and $MA_3Bi_2I_9$ that have a smaller E_B were monitored with a step of 3 °C while for $Cs_3Bi_2Cl_9$ and $Cs_3Bi_2Br_9$ the step was 15 °C. This type of study was previously conducted with a similar approach for the band gap of lead bromide perovskite single crystals.[11,85] In these works, we demonstrated that a lattice phase transition is detectable through SE measurements when a change of slope appears in the energy versus temperature plot of the critical point at the lowest energy.

Figure 2 shows the variation of the second derivative of the real (ϵ_1) and imaginary (ϵ_2) parts of the dielectric function from which the CPs can be extracted in the range −90 °C to 90 °C (with 30 °C temperature step) for $Cs_3Bi_2Br_9$ (Figure 2a,b) and $Cs_3Bi_2I_9$ (Figure 2c,d).

As qualitative evidence, $Cs_3Bi_2Cl_9$ behaves similarly to $Cs_3Bi_2Br_9$ (Figure S10, Supporting Information), whereas $Cs_3Bi_2I_9$ behaves similarly to $MA_3Bi_2I_9$ (Figure S10, Supporting Information).

By lowering the temperature, it is possible to identify a general trend for all Bi-based materials: the E_{ex} peak amplitude (A) increases (y-axis) and the E_{ex} broadening (Γ) decreases (x-axis) (see

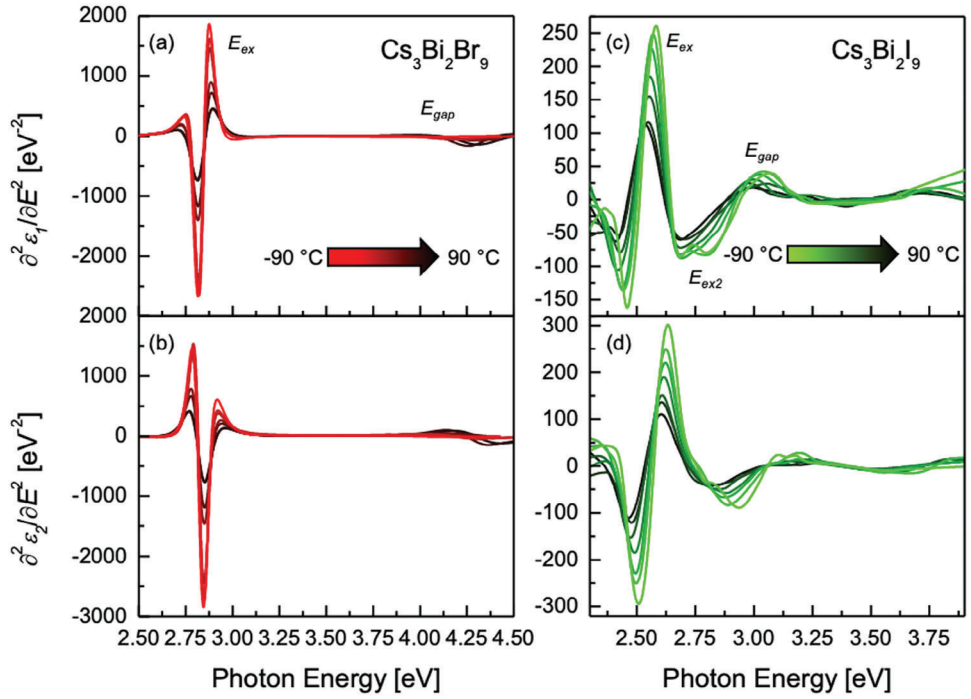

Figure 2. a,b) Second derivative of the real (ϵ_1) and imaginary (ϵ_2) part of the dielectric function across the temperature range from –90 °C to 90 °C ($\Delta T = 30$ °C) for $Cs_3Bi_2Br_9$ and c,d) $Cs_3Bi_2I_9$

also Figures S11–S13, Supporting Information). These findings are consistent with expectations, as exciton–phonon interactions are smaller at lower temperatures, leading to a higher energetic localization of the excitons. Furthermore, the E_{ex} position does not vary significantly with the temperature, in contrast with the E_{gap} position which undergoes significant shifts. Quantifying numerically all these observations is possible through the CP analysis.

Figure 3 shows, within the CP analysis, the temperature dependence of the energy position of E_{ex} and E_{gap} with the EB for Cs3Bi2Cl9 (a–c), Cs3Bi2Br9 (d–f), Cs3Bi2I9 (g–i), and MA3Bi2I9 (j–l). The other CP parameters (A, Γ, Φ) trend versus temperature are reported in the Supporting Information (Figures S11–S13, Supporting Information). We observed that Cs3Bi2Cl9 and Cs3Bi2Br9 samples exhibit similar behavior, notwithstanding the differences in their crystal structure. Specifically, E_{gap} and E_{ex} have a linear dependence in the whole temperature range (Figure 3a,d). In agreement with our previous work,[11] we argue that a linear dependence of the energy with the temperature indicates that no phase transitions occur within the studied temperature interval. Measurements done by differential scanning calorimetry for Cs3Bi2Br9 report a phase transition from hexagonal toward monoclinic phase at −178 °C, which is outside the temperature range here investigated.[86–88]

The temperature dependence of E_{ex} and E_{gap} in both I-based crystals ($Cs_3Bi_2I_9$ and $MA_3Bi_2I_9$) differs from above and it is more complex. For $Cs_3Bi_2I_9$, the E_{ex} curve slope starts to slowly decrease at 45 °C going toward lower temperature and, at ≈−50 °C, there is a net change in the curve slope that we associate with a reversible phase transition (Figure 3g) from the hexagonal to the monoclinic lattice at −53 °C.[57,89] In addition, a second excitonic peak (E_{ex2} in Figure 2e,f) emerges at ≈2.68 eV at the same temperature. The E_{gap} linearly decreases with temperature (Figure 3h), in good agreement with the literature.[57,82] Consequently, E_B decreases linearly, differently from the two previous crystals (Figure 3i). This finding suggests that better performances could be achieved for $Cs_3Bi_2I_9$-based solar cells at the typical operating temperature of 45–85 °C[90] due to the narrowing of the electronic band gap resulting in improved optical absorption and the decrease of E_B causing an improved charge extraction.

The behavior of $MA_3Bi_2I_9$ E_{ex} exhibits an even higher degree of complexity. The E_{ex} value shows a linear increase in the range of temperature 90–25 °C (Figure 3j). However, as the sample is further cooled from 25 °C to ≈−50 °C, the slope gradually decreases down to −90 °C. Similarly to the $Cs_3Bi_2I_9$ sample, we could identify at −50 °C a slope change. This is in good agreement with Jakubas et al.[91] who report a second-order phase transition occurring at −50 °C. We note that Kamminga et al.[92] report that the $MA_3Bi_2I_9$ crystal structure gradually evolves from a hexagonal phase to a monoclinic phase by decreasing the temperature from 27 °C to −113 °C through the alignment of the methylammonium cations along the **b** lattice direction. The trend of E_{gap} with respect to temperature exhibits similarity to the trend of E_{ex} (Figure 3k) and therefore E_B increases with temperature (Figure 3l) as for $Cs_3Bi_2Br_9$, and $Cs_3Bi_2Cl_9$. We note here that notwithstanding $MA_3Bi_2I_9$ shares similar structural characteristics with $Cs_3Bi_2I_9$, their optical properties present some fine differences. An E_{ex2} peak is absent from $MA_3Bi_2I_9$ below the phase transition temperature, whereas the exciton binding energies have different temperature trends. We hypothesize the presence of weakly bound excitons at the conduction band edge that may be responsible for these differences.

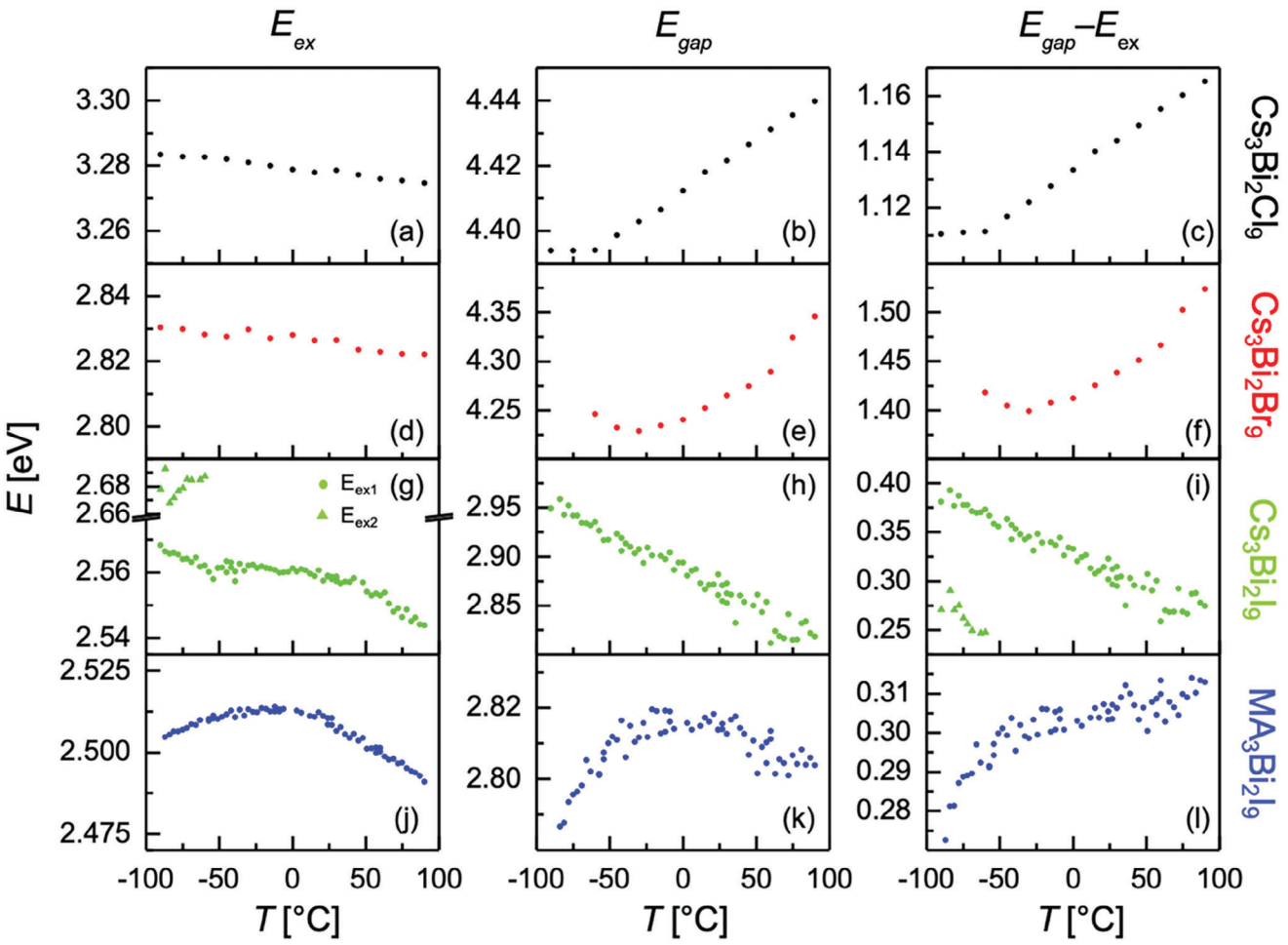

Figure 3. a–c) Energy position of E_{ex} and E_{gap} with E_B=E_{gap} – E_{ex} vs temperature for $Cs_3Bi_2Cl_9$, d–f) $Cs_3Bi_2Br_9$, g–i) $Cs_3Bi_2I_9$, and j–l) $MA_3Bi_2I_9$.

To better interpret the experimental measurements of the optical constants, we performed density functional theory (DFT) calculations for all the experimentally studied systems in their RT phases and post-processed the obtained electronic structure within the Bethe–Salpeter equation (BSE)[93,94] for the calculation of the real and imaginary parts of the dielectric function. We note that the BSE allows for the calculation of the absorption properties considering the interaction between electrons and holes in the excited electronic spectrum, which is important when strong excitonic features are present. A specific requirement for the studied Bi-based materials was the consideration of spin-orbit coupling effects within the calculation scheme, due to their impact on the description of the conduction band of these systems. (Figure S14, Supporting Information).[95,60] Specifically, in the case of $Cs_3Bi_2I_9$, spin-orbit interactions split the lower conduction band into two sub-bands (see $Cs_3Bi_2I_9$ Figure S14a, Supporting Information) whereas for $Cs_3Bi_2Br_9$ they "mix" low-dispersed sub-bands in a single band (see $Cs_3Bi_2Br_9$ in Figure S14b, Supporting Information). In both cases, the qualitative differences in the conduction band introduced by spin-orbit interactions cannot be neglected when evaluating the optical transitions of these materials. Moreover, It is interesting to note that all systems share some common characteristics regarding the main orbital projections in their electronic structure (Figure S15, Supporting Information): conduction bands are strongly characterized by Bi *p* orbitals (with a total angular momentum $J = 1/2$ for lower energies and $J = 3/2$ for higher energies), whereas the valence band maxima are mainly shaped by halide *p*-orbital contributions. The two iodide systems ($Cs_3Bi_2I_9$ and $MA_3Bi_2I_9$) present very similar electronic properties (Figure S16, Supporting Information) arising from the similarity in their structural configuration for a wide range of temperatures. Hereon, only the optical properties of inorganic halides will be discussed. **Figure 4** shows the imaginary part of the dielectric function (ϵ_2) calculated within the BSE theory for the $Cs_3Bi_2I_9$, $Cs_3Bi_2Br_9$ and $Cs_3Bi_2Cl_9$ systems and compares the results with experimental measurements at RT.

All curves show strong excitonic characteristics when electron–hole interactions are considered (red lines) with respect to optical calculations that do not account for excitonic effects (blue lines). The $Cs_3Bi_2I_9$ system is characterized by a main excitonic peak having a slightly higher binding energy compared to the experiment. Additionally, the curve is red-shifted with respect to the one calculated without electron–hole interactions. The case of $Cs_3Bi_2Br_9$ is more particular, as between the dominant excitonic peak and the second optical peak of the experimental curve, intermediate peaks (with the most prominent at ≈3.15 eV)

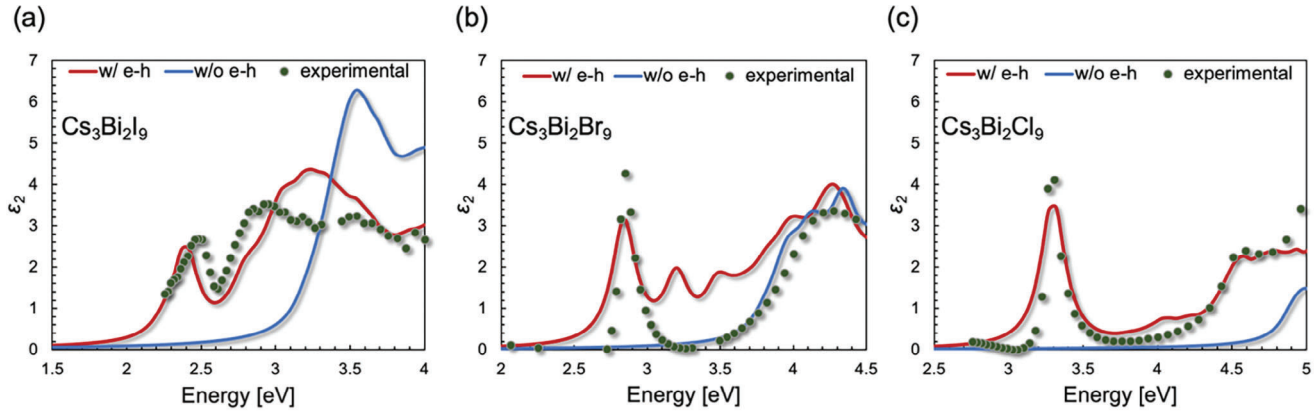

Figure 4. The imaginary part of the dielectric function (ϵ_2) calculated within the BSE theory (red lines) and the independent particle approximation (blue lines) for a) $Cs_3Bi_2I_9$, b) $Cs_3Bi_2Br_9$, and c) $Cs_3Bi_2Cl_9$. Experimental data (green dots) correspond to measurements using SE at RT.

appear only in the calculated spectrum. Similar features have been experimentally observed only in $Cs_3Bi_2Br_9$ nanocrystals at certain crystallographic directions,[96] but are absent from crystals of bigger dimensions. This aspect indicates a rather strong influence of the optical characteristics in this system, either from structural characteristics that are not captured in the simple trigonal model used for our calculations, or from local characteristics that are only present at the nanoscale. Nevertheless, our calculations indicate that these intermediate peaks should be intrinsic to the bulk material and independent of surface-related phenomena. It is also interesting to note that the second peak of the experimental optical spectrum in $Cs_3Bi_2Br_9$ practically coincides with the first peak of the ϵ_2 curve in the independent particle approximation (i.e., without considering electron–hole interactions in the calculation scheme). Finally, an almost excellent agreement between theoretical and experimental data is obtained in the case of $Cs_3Bi_2Cl_9$, showing a strongly redshifted spectrum with respect to the independent particle approximation and a main excitonic peak at ~3.32 eV. Some divergences between the experimental and theoretical data appear only for higher energy values, reflecting the limited number of bands considered for the calculation of the static dielectric matrices (see the Experimental section) with respect to the extremely dense electronic states that are present in the valence band of the material (Figure S12, Supporting Information). Overall, the BSE level of theory appears necessary for the proper estimation of the optical properties of Bi-based halide perovskites.

3. Conclusion

Our multiparameter analysis provides a comprehensive outlook on the behavior of the excitonic band gap and the continuous absorption onset for $A_3Bi_2X_9$ single crystals depending on the temperature. This is crucial for various optoelectronic applications. In particular, we investigated the structural and optical properties of four Bismuth halide single crystals, namely $Cs_3Bi_2Cl_9$, $Cs_3Bi_2Br_9$, $Cs_3Bi_2I_9$, and $MA_3Bi_2I_9$. XRD measurements unveiled their crystalline structure, revealing a quasi 1D orthorhombic structure for $Cs_3Bi_2Cl_9$, a quasi 2D trigonal structure for $Cs_3Bi_2Br_9$ and a quasi 0D hexagonal structure for $Cs_3Bi_2I_9$ and $MA_3Bi_2I_9$. Strong excitonic features were observed for all materials with distinct characteristics, based on the chemical composition of both anions and cations. E_B values for $Cs_3Bi_2Cl_9$, $Cs_3Bi_2Br_9$ and $MA_3Bi_2I_9$ increased with temperature, while for the $Cs_3Bi_2I_9$ the trend was diametrically opposite. We identified a phase transition from the hexagonal to the monoclinic lattice at −53 °C for $Cs_3Bi_2I_9$, and at −50 °C for $MA_3Bi_2I_9$. The wide electronic band gap of $MA_3Bi_2I_9$ (2.81 eV) and of $Cs_3Bi_2I_9$ (2.87 eV) and the high exciton binding energies (≈300 meV) are the main reasons for the low-efficiency values of solar cells, suggesting that focused strategies are required to improve the performances.[74] On the other hand, all Bismuth halide single crystals have a great potential for application as highly efficient photodetectors.

4. Experimental Section

Chemicals and Reagents: Cesium chloride (≥99.999% CsCl, trace metals basis), cesium bromide (99.999% CsBr, trace metals basis), cesium iodide (AnhydroBeads, 99.999% CsI, perovskite grade), bismuth (III) chloride (anhydrous, 99.998% $BiCl_3$, trace metals basis), bismuth (III) bromide (anhydrous, 99.998% $BiBr_3$ trace metals basis), bismuth (III) iodide (≥99.998% BiI_3, trace metals basis), hydrochloric acid (Suprapur, 36% HCl), hydrobromide acid (ACS reagent, 48% HBr), and hydroiodic acid (EMPLURA, 57% HI) were purchased from Sigma–Aldrich. All chemicals were used without further purification.

Preparation of $A_3Bi_2X_9$ Single Crystals: $A_3Bi_2X_9$ single crystals were prepared using the hydrothermal method. The 0.05 M perovskite solutions were prepared by dissolving the precursors CsX and BiX (molar ratio 3:2) in 20 mL of hydrohalic acids (CsCl and BiCl in HCl, etc.) in hydrothermal autoclave reactor. For detailed precursor masses, see Table S1 and Figure S1 (Supporting Information). The solutions were then heated to 200 °C and kept at constant temperature for 2 h to ensure the complete dissolution of the precursors. In the next step, the solutions were cooled down from 200 °C to 25 °C (temperature gradient 1°C h^{-1}) after which millimetre-sized single crystals were obtained. The obtained crystals were then extracted from the solution and separated based on their size and geometry. Samples with the most suitable geometry were used as seeds for further growth. The seeds were placed in the previously filtered perovskite solutions previously filtered (PTFE 0.45 µm) and heated to 50 °C, after which they were slowly cooled down (1°C h^{-1}) to 25 °C. The obtained Bi-based perovskite single crystals had exceptionally flat surfaces that were crucial for the optical characterization that they underwent. Microscopic photos including SEM images and a detailed scheme of the synthetic procedure are presented in Figures S2–S5 (Supporting Information). It is important to observe that excitonic bands function as chromophores, ex-

plaining the crystal's color (white for $Cs_3Bi_2Cl_9$, yellow for $Cs_3Bi_2Br_9$, and reddish for $Cs_3Bi_2I_9$ and $MA_3Bi_2I_9$).

Spectroscopic Ellipsometry: Spectroscopic Ellipsometry (SE) was performed by using a V-VASE, J.A. Woollam equipped with an autoretarder. The measurements have been performed at three angles, 50°, 60°, and 70° below and above the Brewster angle, over a wide range of wavelengths 245–1240 nm (1–5 eV) with steps of 10 nm or less depending on the curve steepness. A wide temperature range of −90 to 90 °C was explored, varying the temperature with an Instec MK100 heater/cooler system with an accuracy of 0.1 °C. Each sample, once aligned, was left in the same position for the whole set of measurements at any temperature to ensure the highest measurement reproducibility. Furthermore, as the sample was transparent in the sub-band gap spectral region, possible backside reflection was avoided by rear surface roughening via sandblasting. This strategy switches off any interference effect that affects optical measurements in the case of transparent substrates. A Kramers–Kronig consistent optical model was built based on multiple critical points parabolic band (CPPB) oscillators to fit experimental data (Ψ and Δ) and determine the real and imaginary parts of the dielectric function (ϵ_1 and ϵ_2). Measurements were collected using a slightly over-pressurized N_2-filled chamber to prevent sample degradation in the air.

X-ray Diffraction: XRD patterns were collected using a SmartLab (Rigaku) diffractometer equipped with a 9 kW rotating anode Cu x-ray source (operating at 45 kV and 200 mA) and HyPix-3000 detector. The step size for pattern recording was 0.01° with an acquisition speed of 0.1° min^{-1}.

Density Functional Theory: The density functional (DFT) theory was used as implemented in the plane-wave Quantum Espresso code[97] to study the electronic and optical properties of hybrid and inorganic bismuth halide crystals. The trigonal phase of $Cs_3Bi_2Br_9$ (space group: P$\bar{3}$m1)[98] was considered, the hexagonal phase of $Cs_3Bi_2I_9$ and $MA_3Bi_2I_9$ (space group: $P6_3/mmc$),[47,99,100] and the orthorhombic phase of $Cs_3Bi_2Cl_9$ (space group: Pnma),[41] which are all found experimentally at room temperature. Unit cell calculations were performed with the Perdew–Burke–Ernzerhof (PBE) exchange-correlation functional[101] along with fully relativistic optimized norm-conserving Vanderbilt pseudopotentials[102] to account for spin-orbit coupling effects that are prominent in bismuth halides.[95,60] Convergence was achieved with a plane-wave cutoff kinetic energy of 50 Ry and an augmented charge density cutoff of 500 Ry, along with a Γ-centered $4 \times 4 \times 2$ Monkhorst–Pack grid[103] for the sampling of the Brillouin zone in the case of $Cs_3Bi_2I_9$ ($MA_3Bi_2I_9$), an $8 \times 8 \times 6$ grid in the case of $Cs_3Bi_2Br_9$ and a $1 \times 3 \times 2$ grid for $Cs_3Bi_2Cl_9$. Both atoms and lattice parameters were allowed to fully relax. The complex dielectric function of the two materials was calculated within the Bethe–Salpeter equation using the YAMBO code.[104,105] The static dielectric matrices were calculated using 32 bands for $Cs_3Bi_2Br_9$, 78 bands for $Cs_3Bi_2I_9$, and 148 bands for $Cs_3Bi_2Cl_9$, while the damping coefficient was set to 0.1 eV for all materials. The PBE Kohn–Sham wave functions were considered for the optical calculations, whereas the obtained ϵ_2 data were rigidly blue-shifted until the onset of the experimental data, to cancel the differences between the experimental and the DFT band gap value. The BSE kernel was built with an energy cutoff of 10 Ry for the components of Hartree potential and 6 Ry for the screened interaction block size.

Supporting Information

Supporting Information is available from the Wiley Online Library or from the author.

Acknowledgements

Authors from Brno University of Technology acknowledge financial support from JCMM Brno Ph.D. Talent, Interfaculty project FCH/FEKT-J-23-8288 and FCH-S-23-8208. The authors also thank Dr. Sarka Tumova from FCH BUT for SEM measurements. Authors from CNR-IMM acknowledge financial support from the European Union (NextGeneration EU) through the MUR-PNRR project SAMOTHRACE – Sicilian MicronanoTech Research and Innovation Center (ECS00000022, CUP B63C22000620005) and the partial support by the national project, BEYOND NANO Upgrade (CUP G66J17000350007).

Conflict of Interest

The authors declare no conflict of interest.

Data Availability Statement

The data that support the findings of this study are available from the corresponding author upon reasonable request.

Keywords

dielectric function, excitonic binding energy, Lead-free perovskites, optical bandgap, single crystal, spectroscopic ellipsometry

Received: September 25, 2023
Revised: November 14, 2023
Published online: December 24, 2023

[1] H. Min, D. Y. Lee, J. Kim, G. Kim, K. S Lee, J. Kim, M. J. Paik, Y. K. K Kim, K. S. Kim, M. G. Kim, T. J. Shin, S. I Seok, *Nature* **2021**, *598*, 444.
[2] Z. Liu, W. Qiu, X. Peng, G. Sun, X. Liu, D. Liu, Z. Li, F. He, C. Shen, Q. Gu, F. Ma, H.-L. Yip, L. Hou, Z. Qi, S.-J. Su, *Adv. Mater.* **2021**, *33*, 2103268.
[3] X. Zhan, X. Zhang, Z. Liu, C. Chen, L. Kong, S. Jiang, S. Xi, G. Liao, X. Liu, *ACS Appl. Mater. Interfaces* **2021**, *13*, 45744.
[4] Y. Park, S. H. Kim, D. Lee, J.-S. Lee, *Nat. Comm.* **2021**, *12*, 3527.
[5] S.-Y. Kim, D. A. Park, N. G., *ACS Appl. Electron. Mater.* **2022**, *4*, 2388.
[6] A. Kojima, K. Teshima, Y. Shirai, T. Miyasaka, *J. Am. Chem. Soc.* **2009**, *131*, 6050.
[7] S. Valastro, E. Smecca, G. Mannino, C. Bongiorno, G. Fisicaro, S. Goedecker, V. Arena, C. Spampinato, I. Deretzis, S. Dattilo, A. Scamporrino, S. Carroccio, E. Fazio, F. Neri, F. Bisconti, A. Rizzo, C. Spinella, A. La Magna, A. Alberti, *Nat. Sustain.* **2023**, *6*, 974.
[8] M. M. Lee, J. Teuscher, T. Miyasaka, T. N. Murakami, H. J. Snaith, *Science* **2012**, *338*, 643.
[9] G. Náfrádi, E. Horváth, M. Kollár, A. Horváth, P. Andricevic, A. Sienkiewicz, L. Forró, B. Náfrádi, *En. Conv. Manag.* **2020**, *205*, 112423.
[10] M. A. Green, A. Ho-Baillie, H. J. Snaith, *Nat. Photonics* **2014**, *8*, 506.
[11] G. Mannino, I. Deretzis, E. Smecca, A. La Magna, A. Alberti, D. Ceratti, D. Cahen, *J. Phys. Chem. Lett.* **2020**, *11*, 2490.
[12] Y. Huang, L. Li, Z. Liu, H. Jiao, Y. He, X. Wang, R. Zhu, D. Wang, J. Sun, Q. Chen, H. Zhou, *J. Mat. Chem. A* **2017**, *5*, 8537.
[13] Z. Xu, H. Li, H. Zhao, Q. Fu, H. Tao, S. Wang, Z. Ma, J. Ding, Y. Ma, Y. Han, *Cryst. Eng. Comm.* **2019**, *21*, 4169.
[14] J. Kang, L.-W. Wang, *J. Phys. Chem. Lett.* **2017**, *8*, 489.
[15] J. Pospisil, O. Zmeskal, S. Nespurek, J. Krajcovic, M. Weiter, A. Kovalenko, *Sci. Rep.* **2019**, *9*, 3332.
[16] J. Pospisil, A. Guerrero, O. Zmeskal, M. Weiter, J. J. Gallardo, J. Navas, G. Garcia-Belmonte, *Adv. Funct. Mater.* **2019**, *29*, 1900881.
[17] B. B. Kadhim, A. Manshad, A.-M. Zamil, *J. Sci.* **2019**, *30*, 174.
[18] S. Gavranovic, J. Pospisil, O. Zmeskal, V. Novak, P. Vanysek, K. Castkova, J. Cihlar, M. Weiter, *ACS Appl. Mat. Interf.* **2022**, *14*, 20159.

[19] Q. Dong, Y. Fang, Y. Shao, P. Mulligan, J. Qiu, L. Cao, J. Huang, *Science* **2015**, *347*, 967.
[20] Y. Chen, H. T. Yi, X. Wu, R. Haroldson, Y. N. Gartstein, Y. I. Rodionov, K. S. Tikhonov, A. Zakhidov, X.-Y. Zhu, V. Podzorov, *Nat. Comm.* **2016**, *7*, 12253.
[21] B. Chen, S. Wang, Y. Song, C. Li, F. Hao, *Chem. Eng. J.* **2022**, *430*, 132701.
[22] Z. Xiao, Z. Song, Y. Yan, *Adv. Mat.* **2019**, *31*, 1803792.
[23] P. Xu, S. Chen, H.-J. Xiang, X.-G. Gong, S.-H. Wei, *Chem. Mat.* **2014**, *26*, 6068.
[24] G. Mannino, J. Sanchez-Diaz, E. Smecca, S. Valastro, I. Deretzis, R. S. Sánchez, J. P. Martinez-Pastor, I. Mora-Seró, A. Alberti, *Sol. RRL* **2023**, *7*, 2300610.
[25] T. Leijtens, R. Prasanna, A. Gold-Parker, M. F. Toney, M. D. Mcgehee, *ACS Energy Lett.* **2017**, *2*, 2159.
[26] C. C. Stoumpos, L. Frazer, D. J. Clark, Y. S. Kim, S. H. Rhim, A. J. Freeman, J. B. Ketterson, J. I. Jang, M. G. Kanatzidis, *J. Am. Chem. Soc.* **2015**, *137*, 6804.
[27] G. Volonakis, M. R. Filip, A. A. Haghighirad, N. Sakai, B. Wenger, H. J. Snaith, F. Giustino, *J. Phys. Chem. Lett.* **2016**, *7*, 1254.
[28] M. R. Filip, S. Hillman, A. A. Haghighirad, H. J. Snaith, F. Giustino, *J. Phys. Chem. Lett.* **2016**, *7*, 2579.
[29] H. Lei, D. Hardy, F. Gao, *Adv. Funct. Mater.* **2021**, *31*, 2105898.
[30] A. Feng, X. Jiang, X. Zhang, X. Zheng, W. Zheng, O. F. Mohammed, Z. Chen, O. M. Bakr, *Chem. Mat.* **2020**, *32*, 7602.
[31] X. Chen, M. Jia, W. Xu, G. Pan, J. Zhu, Y. Tian, D. Wu, X. Li, Z. Shi, *Adv. Optical Mater.* **2023**, *11*, 2202153.
[32] M. Leng, Y. Yang, K. Zeng, Z. Chen, Z. Tan, S. Li, J. Li, B. Xu, D. Li, M. P. Hautzinger, Y. Fu, T. Zhai, L. Xu, G. Niu, S. Jin, J. Tang, *Adv. Funct. Mater.* **2018**, *28*, 1704446.
[33] K. S. Aleksandrov, V. V. Beznosikov, *Phys. Sol. State* **1997**, *39*, 695.
[34] I. P. Aleksandrova, R. Burriel, J. Bartolome, B. S. Bagautdinov, J. Blasco, A. A. Sukhovsky, J. M. Torres, A. D. Vasiljev, L. A. Solovjev, *Phase Trans.* **2002**, *75*, 607.
[35] X. Zheng, W. Zhao, P. Wang, H. Tan, M. I. Saidaminov, S. Tie, L. Chen, Y. Peng, J. Long, W.-H. Zhang, *J. En. Chem.* **2020**, *49*, 299.
[36] H. Zhang, Y. Xu, Q. Sun, J. Dong, Y. Lu, B. Zhang, W. Jie, *Cryst. Eng. Comm.* **2018**, *20*, 4935.
[37] A. Li, M. Yang, P. Tang, X. Hao, L. Wu, W. Tian, D. Yang, J. Zhang, *ACS Appl. Mat. Interf.* **2023**, *15*, 23390.
[38] F. Lazarini, *Acta Cryst. B* **1977**, *33*, 2961.
[39] X. Li, X. Du, P. Zhang, Y. Hua, L. Liu, G. Niu, G. Zhang, J. Tang, X. Tao, *Sci. China Mat.* **2021**, *64*, 1427.
[40] K. Kihara, T. Sudo, *Acta Cryst. B* **1974**, *30*, 1088.
[41] N. K. Tailor, P. Maity, M. I. Saidaminov, N. Pradhan, S. Satapathi, *J. Phys. Chem. Lett.* **2021**, *12*, 2286.
[42] N. K. Tailor, S. Satapathi, *J. Mat. Res. Tech.* **2020**, *9*, 7149.
[43] Y. Cui, L. Yang, X. Wu, J. Deng, X. Zhang, J. Zhang, *J. Mater. Chem. C* **2022**, *10*, 16629.
[44] W.-G. Li, X.-D. Wang, J.-F. Liao, Y. Jiang, D.-B. Kuang, *Adv. Funct. Mater.* **2020**, *30*, 1909701.
[45] A. A. Hussain, A. K. Rana, M. Ranjan, *Nanoscale* **2019**, *11*, 1217.
[46] M. Xia, J.-H. Yuan, G. Niu, X. Du, L. Yin, W. Pan, J. Luo, Z. Li, H. Zhao, K.-H. Xue, X. Miao, J. Tang, *Adv. Funct. Mater.* **2020**, *30*, 1910648.
[47] Y. Zhang, Y. Liu, Z. Xu, H. Ye, Z. Yang, J. You, M. Liu, Y. He, M. G. Kanatzidis, S. Liu, *Nat. Comm.* **2020**, *11*, 2304.
[48] Y. Liu, Y. Gao, J. Zhi, R. Huang, W. Li, X. Huang, G. Yan, Z. Ji, W. Mai, *Nano Res.* **2022**, *15*, 1094.
[49] M. Fox, *Optical Properties of Solids*, Oxford University Press, Oxford **2010**.
[50] R. L. Z. Hoye, J. Hidalgo, R. A. Jagt, J.-P. Correa-Baena, T. Fix, J. L. Macmanus-Driscoll, *Adv. Energy Mater.* **2022**, *12*, 2100499.
[51] E. Smecca, V. Valenzano, S. Valastro, I. Deretzis, G. Mannino, G. Malandrino, G. Accorsi, S. Colella, A. Rizzo, A. La Magna, A. Listorti, A. Alberti, *J. Mater. Chem. A.* **2021**, *9*, 16456.
[52] S. Valastro, G. Mannino, E. Smecca, C. Bongiorno, S. Sanzaro, I. Deretzis, A. La Magna, A. K. Jena, T. Miyasaka, A. Alberti, *Sol. RRL.* **2022**, *6*, 2200008.
[53] B.-W. Park, B. Philippe, X. Zhang, H. Rensmo, G. Boschloo, E. M. J. Johansson, *Adv. Mater.* **2015**, *27*, 6806.
[54] K. K. Bass, L. Estergreen, C. N. Savory, J. Buckeridge, D. O. Scanlon, P. I. Djurovich, S. E. Bradforth, M. E. Thompson, B. C. Melot, *Inorg. Chem.* **2017**, *56*, 42.
[55] S. E. Creutz, H. Liu, M. E. Kaiser, X. Li, D. R. Gamelin, *Chem. Mater.* **2019**, *31*, 4685.
[56] B. Ghosh, B. Wu, H. K. Mulmudi, C. Guet, K. Weber, T. C. Sum, S. Mhaisalkar, N. Mathews, *ACS Appl. Mat. Interf.* **2018**, *10*, 35000.
[57] V. F. Machulin, F. V. Motsnyi, O. M. Smolanka, G. S. Svechnikov, E. Y. Peresh, *Low Temp. Phys.* **2004**, *30*, 964.
[58] T. Kawai, A. Ishii, T. Kitamura, S. Shimanuki, M. Iwata, Y. Ishibashi, *J. Phys. Soc. Jap.* **1996**, *65*, 1464.
[59] N. K. Tailor, S. Satapathi, *J. Phys. Chem. C.* **2021**, *125*, 5243.
[60] S. Rieger, B. J. Bohn, M. Döblinger, A. F. Richter, Y. Tong, K. Wang, P. Müller-Buschbaum, L. Polavarapu, L. Leppert, J. K. Stolarczyk, J. Feldmann, *Phys. Rev. B* **2019**, *100*, 201404.
[61] K. M. Mccall, C. C. Stoumpos, S. S. Kostina, M. G. Kanatzidis, B. W. Wessels, *Chem. Mater.* **2017**, *29*, 4129.
[62] C. W. M. Timmermans, G. Blasse, *J. Lumin.* **1981**, *24/25*, 75.
[63] M. Leng, Y. Yang, K. Zeng, Z. Chen, Z. Tan, S. Li, J. Li, B. Xu, D. Li, M. P. Hautzinger, Y. Fu, T. Zhai, L. Xu, G. Niu, S. Jin, J. Tang, *Adv. Funct. Mater.* **2018**, *28*, 1704446.
[64] M. N. Tran, I. J. Cleveland, E. S. Aydil, *J. Mater. Chem. C.* **2020**, *8*, 10456.
[65] L. Vina, S. Logotheditis, M. Cardona, *Phys. Rev. B* **1984**, *30*, 1979.
[66] S. Logothetidis, L. Vina, M. Cardona, *Phys. Rev. B* **1985**, *31*, 947.
[67] S. Logothetidis, P. Lautenschlager, M. Cardona, *Phys. Rev. B* **1986**, *33*, 1110.
[68] P. Lautenschlager, M. Garriga, S. Logothetidis, M. Cardona, *Phys. Rev. B* **1987**, *35*, 9174.
[69] P. Lautenschlager, M. Garriga, M. Cardona, *Phys. Rev. B* **1987**, *36*, 4813.
[70] P. Lautenschlager, M. Garriga, L. Vina, M. Cardona, *Phys. Rev. B* **1987**, *36*, 4821.
[71] S. Logothetidis, M. Cardona, M. Garriga, *Phys. Rev. B* **1991**, *43*, 11950.
[72] M. Cardona, P. Yu, *Fundamentals of Semiconductors, Physics and Materials Properties*, Springer, Berlin, **2010**.
[73] H. Wu, W. Liu, W. Ma, T. Liang, X. Liu, J. Fan, *Appl. Phys. Lett.* **2022**, *121*, 181902.
[74] F. Ünlü, M. Deo, S. Mathur, T. Kirchartz, A. Kulkarni, *J. Phys.* **2022**, *D 55*, 113002.
[75] J.-C. Hebig, I. Kühn, J. Flohre, T. Kirchartz, *ACS Energy Lett.* **2016**, *1*, 309.
[76] W. Hu, X. He, Z. Fang, W. Lian, Y. Shang, X. Li, W. Zhou, M. Zhang, T. Chen, Y. Lu, L. Zhang, L. Ding, S. Yang, *Nano Energy* **2020**, *68*, 104362.
[77] S. M. Jain, D. Phuyal, M. L. Davies, M. Li, B. Philippe, C. De Castro, Z. Qiu, J. Kim, T. Watson, W. C. Tsoi, O. Karis, H. Rensmo, G. Boschloo, T. Edvinsson, J. R. Durrant, *Nano Energy* **2018**, *49*, 614.
[78] R. J. Elliott, *Phys. Rev.* **1957**, *108*, 1384.
[79] Y. Yang, Y. Yan, M. Yang, S. Choi, K. Zhu, J. M. Luther, M. C. Beard, *Nat. Comm.* **2015**, *6*, 7961.
[80] D. M. Niedzwiedzki, H. Zhou, P. Biswas, *J. Phys. Chem. C* **2022**, *126*, 1046.

[81] S. Rieger, B. J. Bohn, M. Doblinger, A. F. Richter, Y. Tong, K. Wang, P. Muller-Bushbaum, L. Polavarapu, L. Leppert, J. K. Stolarczyk, J. Feldmann, *Phys. Rev. B* **2019**, *100*, 201404.
[82] M. K. Gangishetty, R. W. J. Scott, T. L. Kelly, *Nanoscale* **2016**, *8*, 6300.
[83] G. Mannino, A. Alberti, I. Deretzis, E. Smecca, S. Sanzaro, Y. Numata, T. Miyasaka, A. L. Magna, *J. Phys. Chem. C* **2017**, *121*, 7703.
[84] H. A. Smith, M. Lucas, *Semantic Scholar* **1997**, 19059674.
[85] G. Mannino, I. Deretzis, E. Smecca, F. Giannazzo, S. Valastro, G. Fisicaro, A. La Magna, D. Ceratti, A. Alberti, *J. Phys. Chem. C* **2021**, *125*, 4938.
[86] G. Bator, J. Baran, R. Jakubas, M. Karbowiak, *Vibr. Spectrosc.* **1998**, *16*, 11.
[87] Q. Fan, Y. Ma, H. X., Y. Song, J. Luo, Z. Sun, *Microstruct.* **2022**, *2*, 2022013.
[88] W. Guo, X. Liu, S. Han, Y. Liu, Z. Xu, M. Hong, J. Luo, Z. Sun, *Angewan. Chem.* **2020**, *59*, 13879.
[89] *Z. Kristallogr.* **1999**, *214*, 279.
[90] T. Moot, J. B. Patel, G. Mcandrews, E. J. Wolf, D. Morales, I. E. Gould, B. A. Rosales, C. C. Boyd, L. M. Wheeler, P. A. Parilla, S. W. Johnston, L. T. Schelhas, M. D. Mcgehee, J. M. Luther, *ACS Energy Lett.* **2021**, *6*, 2038.
[91] R. Jakubas, J. Zaleski, L. Sobczyk, *Ferroelectrics* **1990**, *108*, 109.
[92] M. E. Kamminga, A. Stroppa, S. Picozzi, M. Chislov, I. A. Zvereva, J. Baas, A. Meetsma, G. R. Blake, T. T. M. Palstra, *Inorg. Chem.* **2017**, *56*, 33.
[93] G. Onida, L. Reining, A. Rubio, *Rev. Mod. Phys.* **2002**, *74*, 601.
[94] M. Rohlfing, S. G. Louie, *Phys. Rev. B* **2000**, *62*, 4927.
[95] B. Ghosh, S. Chakraborty, H. Wei, C. Guet, S. Li, S. Mhaisalkar, N. Mathews, *J. Phys. Chem. C* **2017**, *121*, 17062.
[96] H. Geng, Z. Huang, H. Geng, S. Liu, M. A. Naumova, R. Salvia, S. Chen, J. Wei, L. Zhang, X. Zou, L. Weijua, X. Cai, M. Yuan, Z. Hu, X. Shen, R. Yu, K. Zheng, S. E. Canton, X. Fu, *Sci. China Mat.* **2023**, *66*, 2079.
[97] P. Giannozzi, S. Baroni, N. Bonini, M. Calandra, R. Car, C. Cavazzoni, D. Ceresoli, G. L. Chiarotti, M. Cococcioni, I. Dabo, A. Dal Corso, S. De Gironcoli, S. Fabris, G. Fratesi, R. Gebauer, U. Gerstmann, C. Gougoussis, A. Kokalj, M. Lazzeri, L. Martin-Samos, N. Marzari, F. Mauri, R. Mazzarello, S. Paolini, A. Pasquarello, L. Paulatto, C. Sbraccia, S. Scandolo, G. Sclauzero, A. P. Seitsonen, et al., *J. Phys. Condens. Mat.* **2009**, *21*, 395502.
[98] L. Clinckemalie, R. A. Saha, D. Valli, E. Fron, M. B. J. Roeffaers, J. Hofkens, B. Pradhan, E. Debroye, *Adv. Opt. Mater.* **2023**, *11*, 2300578.
[99] A. J. Lehner, D. H. Fabini, H. A. Evans, C.-A. Hébert, S. R. Smock, J. Hu, H. Wang, J. W. Zwanziger, M. L. Chabinyc, R. Seshadri, *Chem. Mater.* **2015**, *27*, 7137.
[100] K. Eckhardt, V. Bon, J. Getzschmann, J. Grothe, F. M. Wisser, S. Kaskel, *Chem. Comm.* **2016**, *52*, 3058.
[101] J. P. Perdew, K. Burke, M. Ernzerhof, *Rev. Lett.* **1996**, *77*, 3865.
[102] D. R. Hamann, *Phys. Rev. B* **2013**, *88*, 085117.
[103] H. J. Monkhorst, J. D. Pack, *Phys. Rev. B* **1976**, *13*, 5188.
[104] D. Sangalli, A. Ferretti, H. Miranda, C. Attaccalite, I. Marri, E. Cannuccia, P. Melo, M. Marsili, F. Paleari, A. Marrazzo, G. Prandini, P. Bonfà, M. O. Atambo, F. Affinito, M. Palummo, A. Molina-Sánchez, C. Hogan, M. Grüning, D. Varsano, A. Marini, *J. Phys. Cond. Mat.* **2019**, *31*, 325902.
[105] A. Marini, C. Hogan, M. Grüning, D. Varsano, *Phys. Comm.* **2009**, *180*, 1392.